COMMUNICATION

Check for updates

Thermally responsive spatially programmable soft actuators with multiple response states enabled by Grayscale UV light processing†

Yizong Li, [ID] Sooyeon Noh Coodley, Si Chen, Penghao Dong, [ID] Su Li and Shanshan Yao [ID] *

Soft actuators hold great promise for applications in biomimetic robots, artificial muscles, and drug delivery systems due to their adaptability in diverse environments. A critical aspect of designing thermally responsive soft actuators is to achieve spatially programmable actuation under a global thermal stimulus. Different local actuation behaviors can be encoded in one actuator to enable complex morphing structures for different tasks. However, it is challenging to achieve programmability beyond one or binary states. This work introduces a new grayscale ultraviolet (UV) light processing method to fabricate soft actuators with spatially tunable Young's modulus, enabling multiple programmable states in one actuator. Together with a liquid crystal elastomer actuation layer and a photothermal heating layer, the LCE programming layer with spatially programmable moduli allows different regions of the soft actuator to bend to controllable extents under a global thermal stimulus. Various shape morphing patterns can be encoded using UV photomasks with spatially controlled grayscales. Additionally, caterpillar-inspired robots capable of bi-directional crawling and octopus-arm-inspired structures for object manipulation are demonstrated. This work represents advancements in the programmability of thermally responsive soft actuators, laying the foundation for their applications in advanced soft robotic systems.

New concepts

We present a new concept in soft actuator design: the use of grayscale ultraviolet (UV) light processing to achieve spatially programmable Young's moduli within a single actuator. This method allows for multiple, finely controlled actuation states under a global thermal stimulation, overcoming the binary limitations of traditional methods. Unlike existing strategies that rely on complex material alignments or geometry modifications, our technique uses a single photomask to directly control UV exposure, enabling precise modulation of material stiffness without altering the actuator's physical dimensions. This innovation not only simplifies the fabrication process, but also enhances the functional versatility of soft actuators, making them more adaptable for advanced applications in robotics and biomimetic devices. The ability to program various actuation behaviors within one actuation marks a significant advancement in materials science, providing new insights into the development of multi-functional soft systems that can perform complex tasks with high precision. This concept has the potential to revolutionize the design and application of soft actuators, particularly in fields requiring intricate, programmable deformations.

1. Introduction

There has been burgeoning interest in the exploration of soft actuators that convert diverse external stimuli, including temperature,[1-3] light,[4,5] electric fields,[6] magnetic fields,[7,8] pH,[9] and humidity,[10] into mechanical deformation. Soft actuators are of particular interest for real-world applications due to their inherent properties, such as flexibility, adaptability, versatile locomotion, safety, and operational efficiency.[11,12] Among soft actuators, thermally responsive soft actuators that convert thermal energy to mechanical energy have attracted increasing attention.[13,14] Given the prevalence of temperature variations in diverse environments, thermally responsive actuators have demonstrated capacities to function effectively across a spectrum of conditions. The versatility of thermally responsive actuators is further accentuated by various energy sources that can be employed as stimuli for their activation, such as resistive heating,[1] electromagnetic heating,[15] and optical heating.[16] This characteristic renders temperature-responsive actuators adaptable to both tethered and untethered configurations, enhancing their design flexibility and functionality. Consequently, these actuators find applications in various domains, showcasing their potential for diverse and advanced functionalities, including biomimetic robots, artificial muscles, drug delivery systems, and health monitoring.[11]

A critical aspect of designing thermally responsive soft actuators is to achieve spatially programmable actuation, where

Department of Mechanical Engineering, Stony Brook University, Stony Brook, NY 11794, USA. E-mail: Shanshan.yao@stonybrook.edu

different actuation behaviors can be encoded in one monolithic actuator to enable complex morphing structures for different tasks.[17] Traditional thermally responsive soft actuators can uniformly deform the entire structure under a global thermal stimulus, incapable of spatially separating between actuated and non-actuated domains (Fig. 1(a)).[18–20] This uniform deformation constrains their applicability. To address this limitation, several strategies have been proposed to realize spatially programmable actuation (Fig. 1(b)). One strategy is enabled by local heating, where specific areas are heated at different temperatures while the temperature in other areas remains unchanged.[21] Electrothermal and photothermal are typically used to achieve local heating.[1,21,22] This straightforward programming method simplifies the programming mechanism

but requires either multiple electrodes for heating different regions or a light beam to track the actuator's movements for localized heating.[23] These requirements complicate the actuation structure or the control method. Additionally, environmental temperature variations may affect the performance of programmable actuators based on local heating.[3]

Another strategy to achieve spatially programmable actuation is by local programming, where different regions of the actuator are designed to respond differently to the global heating of the entire structure.[24] This strategy is enabled by programming material properties or actuator geometries (Table S1, ESI†).[3,5,24–26] Among thermally responsive materials, liquid crystal elastomers (LCEs) are commonly used for spatially programmable actuation. LCEs consist of mesogens that
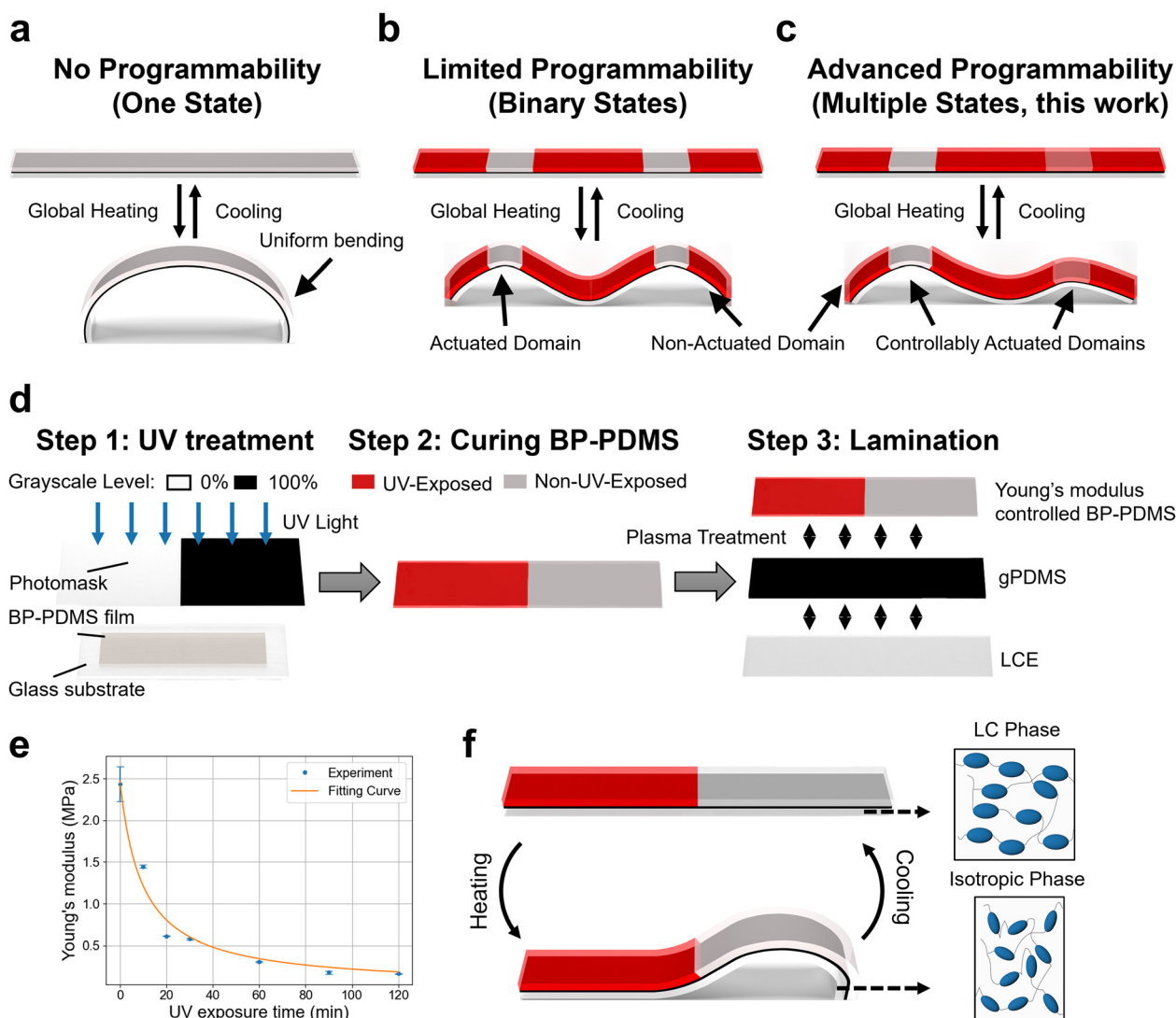

Fig. 1 Fabrication and programmability of the SPSA. (a) The actuator demonstrates uniform bending under global heating, indicating a lack of programmability. (b) The actuator demonstrates limited programmability, which can achieve only two distinct states (active and intact states). (c) The actuator in this work possesses advanced programmability, achieving multiple programmed states under global heating. (d) The fabrication process of the SPSA. The preparation of gPDMS and LCE is detailed in the Experimental section. (e) Young's moduli of BP−PDMS as a function of UV exposure time at an intensity of 1.95 mW cm^{-2}. UV treatments were performed with a fully transparent photomask (grayscale 100%). (f) Schematic of the programmability of the SPSA.

can be aligned and immobilized through polymer chain cross-linking.[27–30] When the temperature reaches a transition threshold, LCEs undergo controlled contraction or extension along the alignment direction.[30] Two principal methods for achieving actuation programmability in LCEs include the precise control of mesogen alignment[27,28,31] and the spatial regulation of crosslink density.[32–34] For example, the crosslink density in LCEs can be increased by post-ultraviolet (UV) treatment after swelling the LCE in a dichloromethane (DCM) solution.[32] A higher crosslink density results in greater strain under the same thermal conditions. By controlling the post-UV treatment through a photomask, the crosslink density of LCEs can be spatially patterned, thereby enabling programmable actuation. Photomasks can also be used to separate between the monodomain (aligned mesogens) and polydomain (unaligned mesogens) regions in LCEs.[27] Under uniaxial stretching, mesogens align along the stretching direction, and UV treatment can fix this alignment, endowing the LCE with a reversible shape memory mechanism, while mesogens in non-UV-exposed region remain unaligned. Consequently, the alignment of mesogens in LCEs can be controlled through varying photomask patterns, allowing the programmed response of LCEs to global heating. However, this approach has primarily explored only two types of regions (actuation and non-actuation domains), thereby limiting programmability to binary states and leaving the full potential of photomask-enabled programmability in thermally responsive soft actuators underexplored.

Efforts have also been devoted to developing programmable actuators by controlling geometries of thermally responsive soft actuators made from materials that exhibit anisotropic properties, such as the coefficient of thermal expansion (CTE) and electrical resistance.[6,35–37] For instance, utilizing materials with anisotropic CTEs enables precise control of the actuator's bending angle by adjusting the orientation between the actuator's longitudinal axis and the direction of the material's higher CTE.[35,37] However, for actuators based on materials with anisotropic CTEs, the bending angle could not be controlled independently without causing twisting. Another example involves aligned carbon nanotube sheets with anisotropic conductivities, which influences the local temperature and bending behavior under electrothermal heating.[6] By adjusting the actuator orientations, the actuation and non-actuation domains can be programmed in one actuator, with the actuation domain oriented perpendicular to the CNT alignment and the non-actuation domains parallel to the CNT alignment. Nevertheless, the programming mechanism is limited to the tethered actuation method and it remains challenging to enable different actuation performance in one actuator.

Despite these advances, the programmability of soft thermal actuators remains limited.[23] Most actuators can only be programmed to exhibit binary states (active and intact) under specific external stimuli (Fig. 1(b)).[38,39] Table S1, ESI† summarizes representative thermally responsive spatially programmable soft actuators. Some efforts have been made to achieve multiple states in one actuator, enabling varying extents of deformation in different regions of the actuator (Fig. 1(c)).[40,41] For example, LCEs can be spatially programmed to exhibit multiple states under global heating by spatially controlling UV exposure time that affects the depth of decrosslinked region.[29] Upon heating, the crosslinked regions contract, while the decrosslinked regions do not exhibit reversible actuation strain, causing the LCE to bend due to the strain mismatch across the thickness. By modulating the depth of the decrosslinked region, the LCE can be programmed to achieve different bending curvatures upon heating. However, lateral programming of the actuator into non-actuation domains remains unachievable, as bending persists even after 6 h of UV exposure. Moreover, this approach requires multiple photomasks to introduce varied UV exposure times for specific spatially controlled actuation, complicating the fabrication process. Additional strategies primarily involve geometric modifications (*e.g.*, thickness of active or passive layers), which may impose constraints on actuator dimensions.[40,41] Thus, developing novel material systems to enhance the spatial programmability of soft actuators is essential for advancing thermally responsive soft actuators.

In this paper, we propose a new grayscale UV light processing method to fabricate Young's modulus-controlled spatially programmable soft actuators (SPSAs). The use of masks with controlled grayscale imparts direct control over UV exposure density, enabling the treatment of the actuator with multiple levels by a single photomask. This allows SPSAs to exhibit different local actuation behaviors in one monolithic actuator under a global thermal stimulus. To the best of our knowledge, no previous work has attained SPSAs by controlling local Young's moduli. Moreover, the grayscale UV processing method allows precise control over the size, number, location, Young's modulus, and the bending behavior of the actuator. Compared with other material or geometry-enabled programming material systems, the reported grayscale UV light processing and Young's modulus modulation method is simple, scalable, not constrained by material alignment, and does not alter the dimensions of the actuator. The proposed actuator comprises three layers: LCE actuation layer, graphite-PDMS (gPDMS) photothermal heating layer, and benzophenone–poly(dimethylsiloxane) (BP–PDMS) programming layer. We selected LCE as the active actuation layer owing to its large negative actuation strain, which results in large bending curvatures in the actuator. Graphite is introduced into PDMS to enhance the heating efficiency and uniformity of the actuator under infrared light. Employing UV photomasks with spatially controlled grayscales, BP–PDMS can be spatially patterned with varying moduli ranging from 0.16 to 2.44 MPa, allowing different regions of the soft actuator to bend to different extents under a global temperature. To demonstrate the programmability, various shape morphing patterns were designed and encoded using grayscale UV light processing. In particular, caterpillar-inspired soft robots are demonstrated by controlling the body curvature, which are capable of crawling in two directions. Furthermore, soft actuators inspired by the movement of an octopus arm are programmed to catch and coil around objects.

2. Results and discussions

2.1.   Design and fabrication of the SPSA

The SPSA is a tri-layer structure consisting of a BP–PDMS layer, gPDMS layer, and LCE layer. LCE is selected as the active layer due to its large negative actuation strain arising from the LC phase-isotropic transition. When heated above the transition temperature, the LCE layer shrinks with a strain of -42% (Fig. S1, ESI†). To provide the required actuation temperature for LCE, PDMS doped with graphite particles is used as the photothermal heating element. Graphite particles are introduced to improve the heating uniformity and efficiency, due to their excellent thermal conductivity, mechanical compliance, and low cost.[42,43] The programmability is achieved by controlling the Young's modulus of the BP–PDMS layer through UV treatment. Both gPDMS and BP–PDMS exhibit large thermal expansion under heating and induce an enhanced thermal mismatch at their interface, which improves the bending curvature under heating.

The bending curvature of the SPSA can be calculated as:[19,38]

$$k = \frac{6(X_{12} + X_{13} + X_{23})}{t_1(1 + Y_2 + Y_3 + Y_{23})} \tag{1}$$

where

$$X_{12} = m_2 n_2 (1 + m_2)(\alpha_1 - \alpha_2)(T - T_0) \tag{2}$$

$$X_{13} = m_3 n_3 (1 + 2m_2 + m_3)(\alpha_1 - \alpha_3)(T - T_0) \tag{3}$$

$$X_{23} = m_2 n_2 m_3 n_3 (m_2 + m_3)(\alpha_2 - \alpha_3)(T - T_0) \tag{4}$$

$$Y_2 = 4m_2 n_2 + 6m_2^2 n_2 + 4m_2^3 n_2 + m_2^4 n_2^2 \tag{5}$$

$$Y_3 = 4m_3 n_3 + 6m_3^2 n_3 + 4m_3^3 n_3 + m_3^4 n_3^2 \tag{6}$$

$$Y_{23} = m_2 m_3 n_3 [(4m_2^2 + 6m_2 m_3 + 4m_2^3)n_2 + 12(1 + m_2 + m_3)] \tag{7}$$

Here the BP–PDMS layer, gPDMS layer, and LCE layer are represented with subscripts 1, 2, and 3 respectively. α indicates the coefficient of thermal expansion. T_0 and T represent the room temperature and the current temperature respectively. t is the thickness and E is Young's modulus of the corresponding layer. $m_i = t_i/t_1$, and $n_i = E_i/E_1$ for $i = 1, 2, 3$.

Under near-infrared (nIR) irradiation, the temperature of the gPDMS layer increases due to the absorbed nIR energy (Fig. S2, ESI†), which further heats up the entire SPSA. The BP–PDMS and gPDMS expand due to thermal expansion, while the LCE layer contracts. The mismatch between strains of each layer further induces a bending motion of the SPSA. From eqn (1), in addition to temperature, the bending curvature is affected by several parameters: (1) CTEs of each layer, (2) the geometry of each layer, (3) the Young's modulus of each layer. The temperature (through modulating the material resistance),[6] CTEs,[35] and geometry,[36] have been previously explored to spatially program the bending angles of thermal actuators. However, these methods are constrained by several limitations, including the tethered actuation, the inability to independently control the bending angle without inducing twisting, complex fabrication processes, and challenges in achieving multiple actuation states in one actuator. In this work, we program the bending curvatures by controlling Young's moduli of the BP–PDMS layer by a scalable UV light processing method. By employing photomasks with varied grayscale levels, the UV treatment intensities are modulated to encode different moduli across a single actuator. As a result, the spatially programmed BP–PDMS modulus further leads to programmable local bending curvatures of the SPSA under a global temperature.

Fig. 1(d) illustrates fabrication processes of the SPSA. Briefly, benzophenone (BP) flakes are dissolved in xylene and mixed with poly(dimethylsiloxane) (PDMS) precursor. The resultant mixture, BP–PDMS, is subjected to controlled UV light exposure through a photomask with spatially designed grayscale levels (Fig. 1(d) step 1). This irradiation induces the formation of BP radicals that interact with the silicon hydride groups of the curing agent monomers.[44] This interaction effectively inhibits the cross-linking reaction within the exposed region, thereby resulting in a low Young's modulus in the exposed region (Fig. 1(d) step 2). In contrast, in the unexposed region, the cross-linking reaction remains unaltered, maintaining the original relatively high Young's modulus. As shown in Fig. 1(e) and Fig. S3, ESI†, the Young's modulus of the UV-exposed region can be as low as 0.16 MPa, after 120 min of UV treatment at an intensity of 1.95 mW cm^{-2} with a fully transparent photomask (grayscale 100%). The modulus is 15 times smaller than that of regions without UV treatment.

The LCE layer was synthesized *via* a two-stage thiol-acrylate Michael addition and photopolymerization.[1,45,46] A permanently programmed monodomain within the LCE layer was achieved by subjecting the LCE strip to a mechanical stretching at 100% strain, followed by UV exposure. Graphite, at a weight ratio of 12%, was incorporated into PDMS to create the gPDMS layer, due to its good heating efficiency that improves the bending rate (Fig. S2, ESI†). More details on the fabrication of LCE and gPDMS are provided in the Experimental section. Finally, the surfaces of three layers were plasma-treated to enhance the adhesion and subsequently bonded together underwater to minimize air gaps and reduce stress induced during the lamination process (Fig. 1(d) step 3).[47,48] The bonding between each layer is strong and durable, as demonstrated by cyclic actuation tests (Fig. S4, ESI†). The actuation stress of up to 53 KPa (Fig. S5, ESI†) was achieved. The resulting SPSA is programmable, as illustrated in Fig. 1(f). Upon heating above the transition temperature, the LCE layer transitions from the LC phase to the isotropic phase, causing a significant negative strain. The contraction in LCE, together with the thermal expansion of gPDMS and BP–PDMS, results in a high bending curvature of regions with non-UV-exposed BP–PDMS (higher modulus), while the regions with UV-exposed BP–PDMS (lower modulus) remain relatively flat.

2.2.   Programmable performance of the SPSA

The performance of the programmable actuators is mainly determined by the thickness of each layer, Young's modulus

Materials Horizons

Communication

of the BP–PDMS layer, and heating temperature. For better programmability, the following two parameters should be maximized: (1) the maximum curvature achieved and (2) the difference in bending curvatures between UV-exposed regions (through a photomask with 100% grayscale) and non-UV-exposed regions (through a photomask with 0% grayscale). This way, through photomasks with spatially varied grayscale levels (within 0% to 100% grayscale), the actuation behavior in the actuator can be programmed to exhibit actuation with different extents. To characterize the effect of the thickness of each layer on the programmability, a series of parametric studies was conducted. Fig. 2 and Fig. S6, ESI† present the measured curvature differences between UV-exposed (100% grayscale photomask) and non-UV-exposed (0% grayscale photomask) samples with different thicknesses of each layer. First, we investigated the effect of BP–PDMS and LCE layer thickness on bending curvature, where the gPDMS layer was kept at 50 μm thick. It is known that Young's modulus of BP–PDMS is thickness-dependent for layers thicker than 220 μm, as UV radiation cannot penetrate such thickness.[44] Therefore, BP–PDMS thicknesses ranging from 50 to 200 μm were investigated. The thickness of the LCE layer ranged from 150 to 450 μm. As shown in Fig. 2(a)–(c) and Fig. S6a–c, ESI,† increasing the LCE layer thickness resulted in a decrease in both overall bending curvatures and curvature differences between

UV-exposed and non-UV-exposed regions. The maximum curvature of 2.77 cm^{-1} in the non-UV-exposed region and the maximum curvature difference of 1.18 cm^{-1} were achieved with a BP–PDMS layer thickness of 150 μm and a thickness ratio of 1:1 between the BP–PDMS layer and LCE layer. Next, we investigated the effect of gPDMS layer thickness on bending curvature. As shown in Fig. 2(d) and Fig. S6d, ESI,† when the gPDMS thickness was smaller than the BP–PDMS thickness, the Young's modulus of BP–PDMS played a more significant role in determining bending curvature. This resulted in larger curvature differences between UV-exposed and non-UV-exposed regions. However, as the gPDMS thickness increased, the modulus of the gPDMS layer began to dominate the bending curvature of the SPSA, reducing the influence of BP–PDMS Young's modulus. Since the Young's modulus of the gPDMS layer (Fig. S7, ESI†) is smaller than that of BP–PDMS (Fig. S3, ESI†), this led to smaller overall bending curvature and reduced curvature differences (Fig. 2(d)). The results (Fig. 2(d) and Fig. S6d, ESI†) indicate that with a gPDMS thickness of 50 μm, both the maximum curvature achieved and the curvature differences between the UV-exposed and non-UV-exposed regions are realized. The gPDMS thickness of 50 μm was thus selected.

The above discussion is for actuators fabricated using fully UV transparent (100% grayscale) or fully opaque (0% grayscale) photomasks. By employing a photomask with spatially
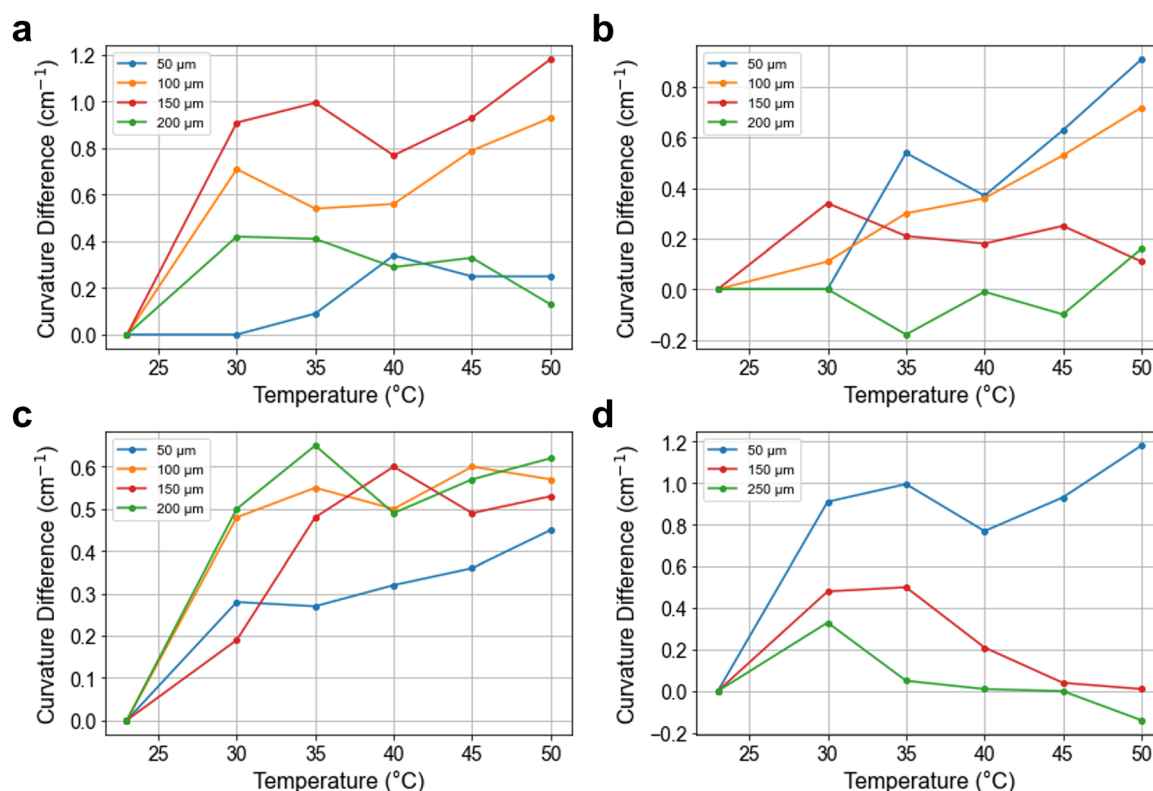

Fig. 2 Curvature differences between SPSAs with the UV-exposed and non-UV-exposed BP–PDMS. (a)–(c) Curvature differences as a function of temperature for a gPDMS layer thickness of 50 μm and BP–PDMS layer thicknesses ranging from 50 to 200 μm, with LCE layer thicknesses of (a) 150 μm, (b) 300 μm, and (c) 450 μm. (d) Curvature differences as a function of temperature for BP–PDMS and LCE layer thicknesses of 150 μm, and gPDMS layer thicknesses ranging from 50 to 250 μm.

modulated grayscale levels, the Young's modulus of BP–PDMS can be varied spatially across the actuator, such that the bending behavior in different regions can be locally encoded by the grayscale of the photomask. The image encoded on the photomask with different grayscale levels modulates the transmittance to the 365 nm UV light (Fig. S8, ESI†). Under the same UV exposure time and intensity, the UV dose that the precursor of BP–PDMS receives is thus modulated, leading to controlled cross-linking levels and Young's moduli of BP–PDMS (Fig. 3(a) and Fig. S9, ESI†). The increase in the grayscale level increases the UV dose delivered to the BP–PDMS. As a result, the Young's modulus becomes smaller and hence the resulting bending curvature of the actuator decreases (Fig. 3(b) and Fig. S10, ESI†). The analysis of work capacity of SPSAs with BP–PDMS layers treated by photomasks of varying grayscale levels is provided in the ESI.†

When a region prepared by the smaller-grayscale photomask is used as a bending joint while the other regions are fabricated using a larger-grayscale photomask, local bending curvatures can be programmed around the bending joint. The bending curvature can be controlled either by changing the dimension of the bending joint or by modulating the grayscale levels used for UV-treating the bending joint. Fig. 4 presents the bending behavior of actuators with different lengths of bending joints, which were prepared without UV treatment (0% grayscale photomask). The results reveal a larger bending curvature for a longer bending joint. When the length of the bending joint is maintained at 8 mm, different local bending behaviors can also be programmed by adjusting the grayscale level of the photomask used for preparing the bending joint (Fig. 5(a)–(c)). As the grayscale level of the photomask increases, Young's modulus of the BP–PDMS layer decreases, causing the joint to exhibit a greater tendency for shrinkage rather than bending, thereby reducing the bending curvature.

To demonstrate the enhanced programmability and complex shape morphing of SPSA, a series of configurations was achieved through the rational design of grayscale levels on the photomask. The grayscale UV processing allows precise control over the size,

number, location, and Young's modulus of the bending joints (Fig. 5(d)–(g)). Four grayscale levels were selected: 0%, 15%, 30%, and 100%. The regions of the BP–PDMS layer treated with a 100% grayscale level were designated as intact parts, as the lower Young's modulus in these areas prevents significant bending, keeping them flat (Fig. 3(b) and Fig. S6, ESI†). The regions treated with 0%, 15%, and 30% grayscale levels served as bending joints, with smaller grayscale levels producing larger bending curvatures and resulting in stronger bending joints. The nIR light heating raises the SPSA temperature to approximately 35 °C. This heating temperature is selected to minimize the influence of thermal effects on the Young's modulus of the BP–PDMS layer. The Young's modulus of the BP–PDMS layer varies by only 4% between room temperature and 40 °C.[44] In contrast, Young's modulus varies significantly by 93% (from 2.44 MPa to 0.16 MPa) due to UV treatments. The low heating temperature ensures minimal impact on both the bending curvature and the programmability of the SPSA. In the first configuration, a bending joint (20 mm by 5 mm) was fabricated by a photomask with a grayscale level of 0% on the right side (Fig. 5(d)). The bending joint was thus positioned on the right side with the LCE layer facing downward. The resulting actuator could quickly change its configuration to a laying down hook shape upon nIR light irradiation and recover to a flat shape when the nIR light was turned off. In Fig. 5(e), a series of bending joints (15 mm by 5 mm) was connected in series. The bending joints were fabricated by a photomask with gradually decreased grayscale levels of 30%, 15%, and 0%. The actuator morphed into a laying down hook shape with smoother transitions between adjacent regions upon nIR light irradiation, due to the gradient grayscale levels. Furthermore, an actuator with two bending joints of the same size (8 mm by 5 mm) was fabricated (Fig. 5(f)). Grayscale levels of 0% and 30% were used to perform the UV treatment for the two bending joints and they were symmetrically positioned with a gap of 19 mm. The SPSA could switch its appearance between a flat and an "M" shape by turning the nIR light on and off. The arch of the "M" shape can be controlled by the grayscale levels. As shown in Fig. 5(f), the bending joint with a grayscale level of 30% has a smaller arch than that
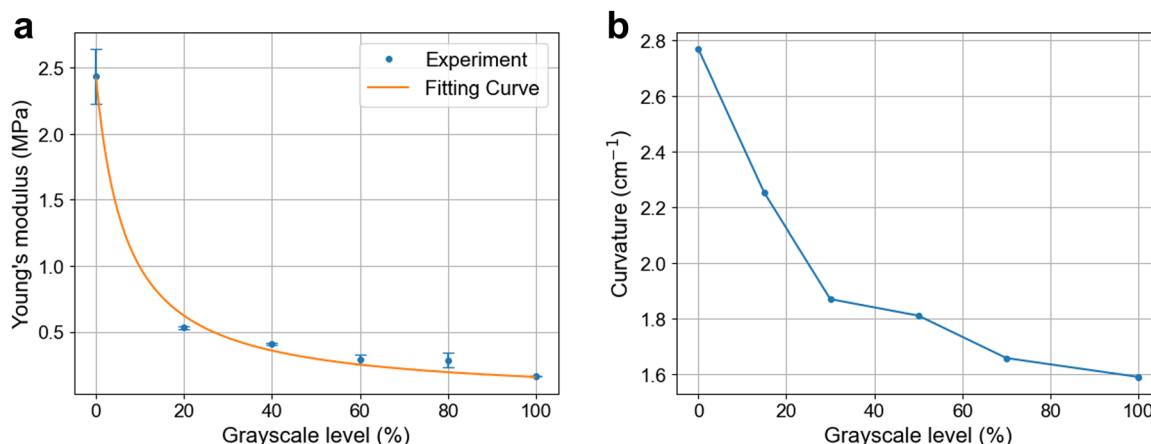

Fig. 3 Grayscale level controlled UV processing. (a) Young's moduli of BP–PDMS layers prepared by photomasks with different grayscale levels. (b) Curvatures of the actuator at 50 °C as a function of grayscale levels. The UV exposure time and UV intensity are maintained the same.
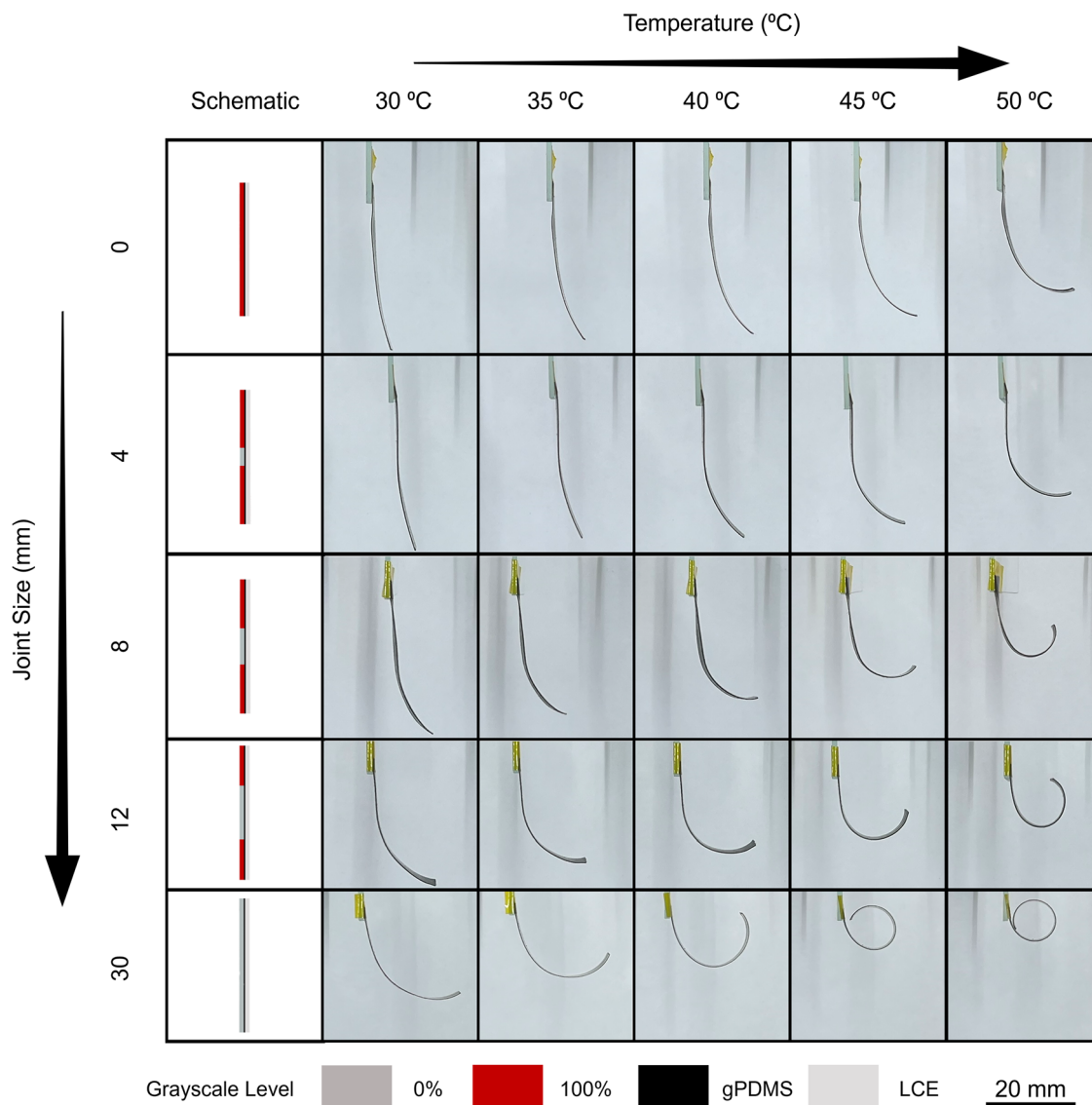
Fig. 4 Effects of the size of the bending joint on the bending curvature of SPSAs at different heating temperatures.

of the bending joint with a grayscale level of 0%. Finally, three bending joints with grayscale levels of 0%, 15%, and 30% were integrated into the actuator (Fig. 5(g)). Under the nIR light irradiation, the SPSA changed its shape from flat to a "trefoil arch" shape. The arch gradually decreased, corresponding to the increase of grayscale levels used to treat the bending joints.

2.3. Bioinspired soft robots enabled by the SPSA

The SPSA exhibits excellent programmability in response to thermal stimuli, making it suitable for applications in soft crawling robotics. This programmability allows the SPSA to be configured with various locomotion modes while maintaining the same initial shape. Here, we first demonstrated two caterpillar-inspired crawling robots that achieve different locomotion directions by controlling the pattern of the BP–PDMS layer. In nature, the Pleurotya caterpillar exemplifies bidirectional locomotion (Fig. 6(a) and (b)).[1,49] The critical mechanism

underlying this bidirectional movement is the precise modulation of body curvatures.[11] More details on the locomotion mechanism can be found in previous papers.[1,11] Though the kinematics of the caterpillar involve complex and segment-specific active control, SPSA shows the capability of locally modulated body curvatures to effectively emulate these forward and backward locomotion modes.

Fig. 6(c)–(e) illustrate the forward and backward crawling enabled by two patterns programmed with different grayscale levels. Additional patterns that enable forward and backward locomotion modes are provided in Fig. S11, ESI.† To realize the forward locomotion mode (Fig. 6(d)), two smaller bending joints were incorporated in series (Fig. 6(c)). The pattern was fabricated by a photomask with a gradient grayscale level of 0%, 15%, and 100%. The size of the bending joint treated with a grayscale of 0% is two times longer than that of the bending joint treated with a grayscale of 15%. The series connected
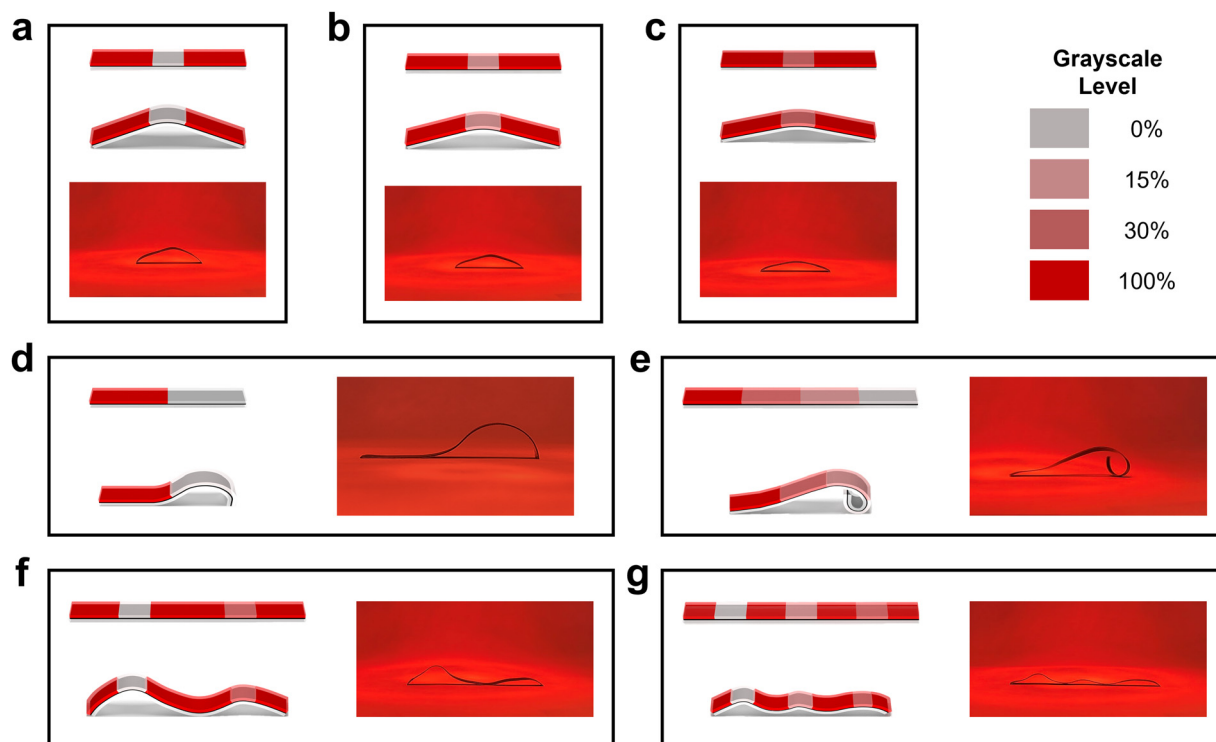
Fig. 5 The programmability of the SPSA under global heating by the nIR light for 2 s. (a)–(c) Bending curvatures as grayscale levels of the UV photomask for preparing the bending joint gradually increase from (a) 0%, (b) 15%, to (c) 30%. (d)–(g) Examples of more complex shape changes and programmability through UV photomasks with spatially programmed grayscales, including (d) laying down hook, (e) smoother laying down hook, (f) M shape, and (g) trefoil arch shape. The LCE layers were facing downward for all configurations.

bending joints were positioned at its tail and when the nIR light was turned on, an asymmetric arc shape was formed. While the other part treated with a grayscale of 100% remains relatively flat upon nIR heating. Under global nIR heating, both the tail and head of the SPSA tend to contract towards its center. The frictional forces to the substrate at the tail (f_{tail}) and head (f_{head}) increase. Because of the asymmetry of the arc shape at the tail and a sufficiently large area with negligible bending curvatures at the head, the tail end surpasses the sliding friction first. As a result, the tail bends forward while the head stays intact. When the nIR light is turned off, the recovery of the asymmetric arc shape induces a larger threshold for sliding friction at the tail end than that at the head end, due to the larger contact angle between the tail end and the ground. Hence, the tail propels the head to move forward while the tail end anchors to the substrate.

To achieve the backward locomotion mode (Fig. 6(e)), larger bending joints and smaller intact parts were incorporated into the actuator (Fig. 6(c)). Similarly, the pattern was fabricated by a photomask with grayscale levels of 0%, 15%, and 100%, and two bending joints were connected in series. When the nIR light is turned on, the middle part of the SPSA lifts more significantly. This occurs because the bending joint treated with 0% grayscale level is longer than that of SPSA in the forward locomotion mode, while the intact part treated with 100% grayscale level is shorter. Hence, the contact area between the head end and the ground becomes smaller, causing f_{head} to

surpass the sliding friction first. As a result, the head end moves backward while the tail end is anchored to the ground. When the nIR light is turned off, the head end stays anchored to the ground and the tail end moves backward, because f_{tail} surpasses the sliding friction first.

Shape changing between coiling and uncoiling states is a common behavior among animals, such as snakes, caterpillars, snails, and octopuses. This shape change can function as a defense mechanism, locomotion method, or feeding and hunting strategies.[50–52] Specifically, the octopus utilizes its arms to catch the prey by coiling its arms around it. To achieve a coiling shape, the octopus arm bends from its tip toward the end of the arm and the curvature propagates gradually.[50,53] To replicate the movement of the octopus's arm, we designed a thermal actuator that can quickly and reversibly change its appearance between coiling and uncoiling shapes upon heating and cooling. To achieve curvature propagation, a photomask with linearly decreased gradient grayscale levels was used to treat the BP–PDMS (Fig. 7(a)). The resulting Young's modulus of the BP–PDMS layer increases gradually from its end to its tip. Under the nIR illumination, the tip of the SPSA bends first, and the curvature propagates towards the end of the arm (Fig. 7(b)). To demonstrate the capability of catching objects, the actuator was utilized to catch a cylinder load that was 15 times heavier than the actuator. As shown in Fig. 7(c), the actuator is able to catch and coil the load upon the nIR irradiation, mimicking the capability of the octopus's arm.
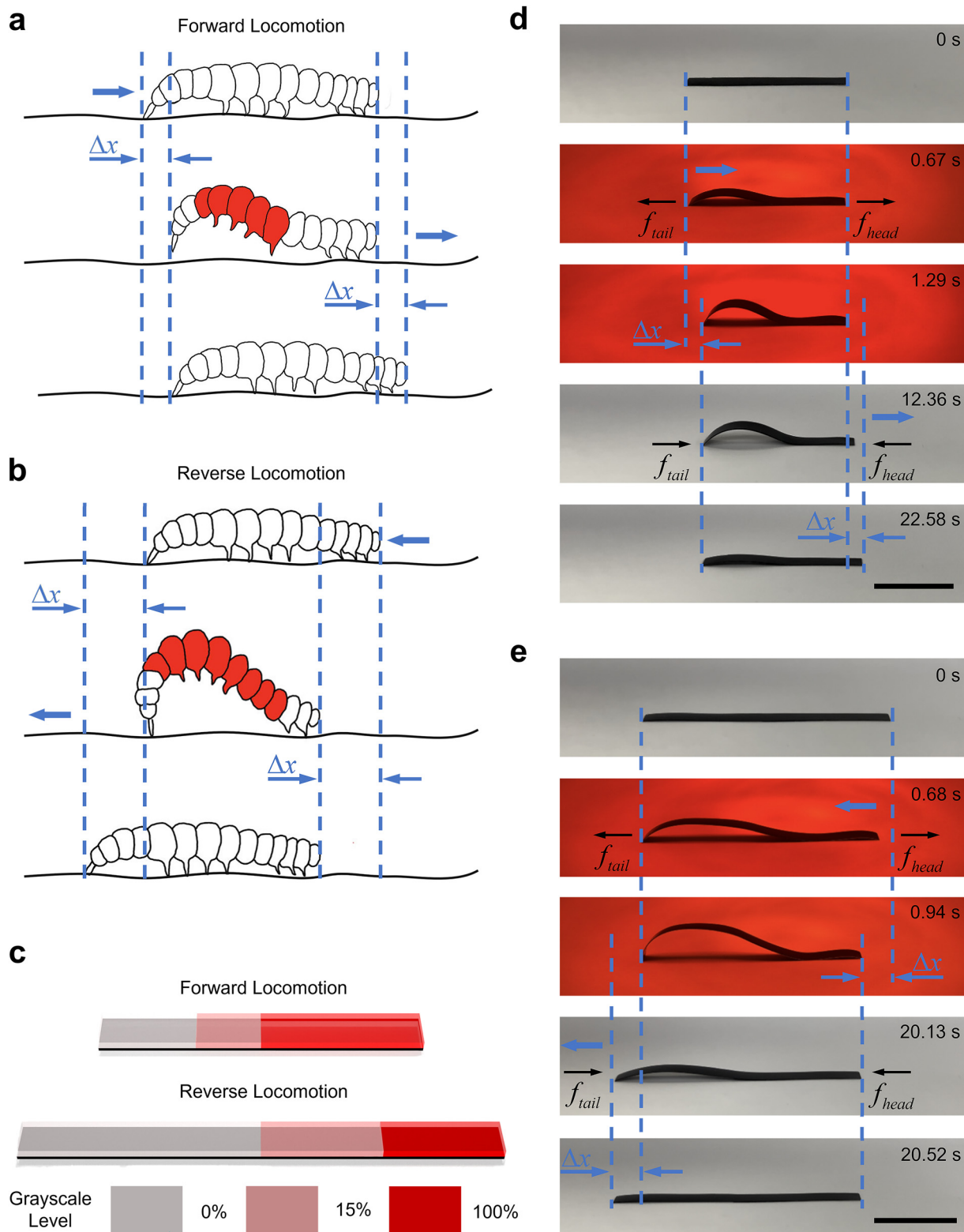
Fig. 6 Caterpillar-inspired soft crawling robots demonstrating locomotion under global heating using an nIR light. (a) and (b) Schematics showing the forward and backward locomotion modes of the caterpillar. (c) Two patterns of the soft crawling robot enabling forward and backward locomotion. Snapshots of (d) forward and (e) backward locomotion modes of the soft crawling robots, actuated by intermittently turning on and off the nIR lamp. Scale bars: 20 mm.
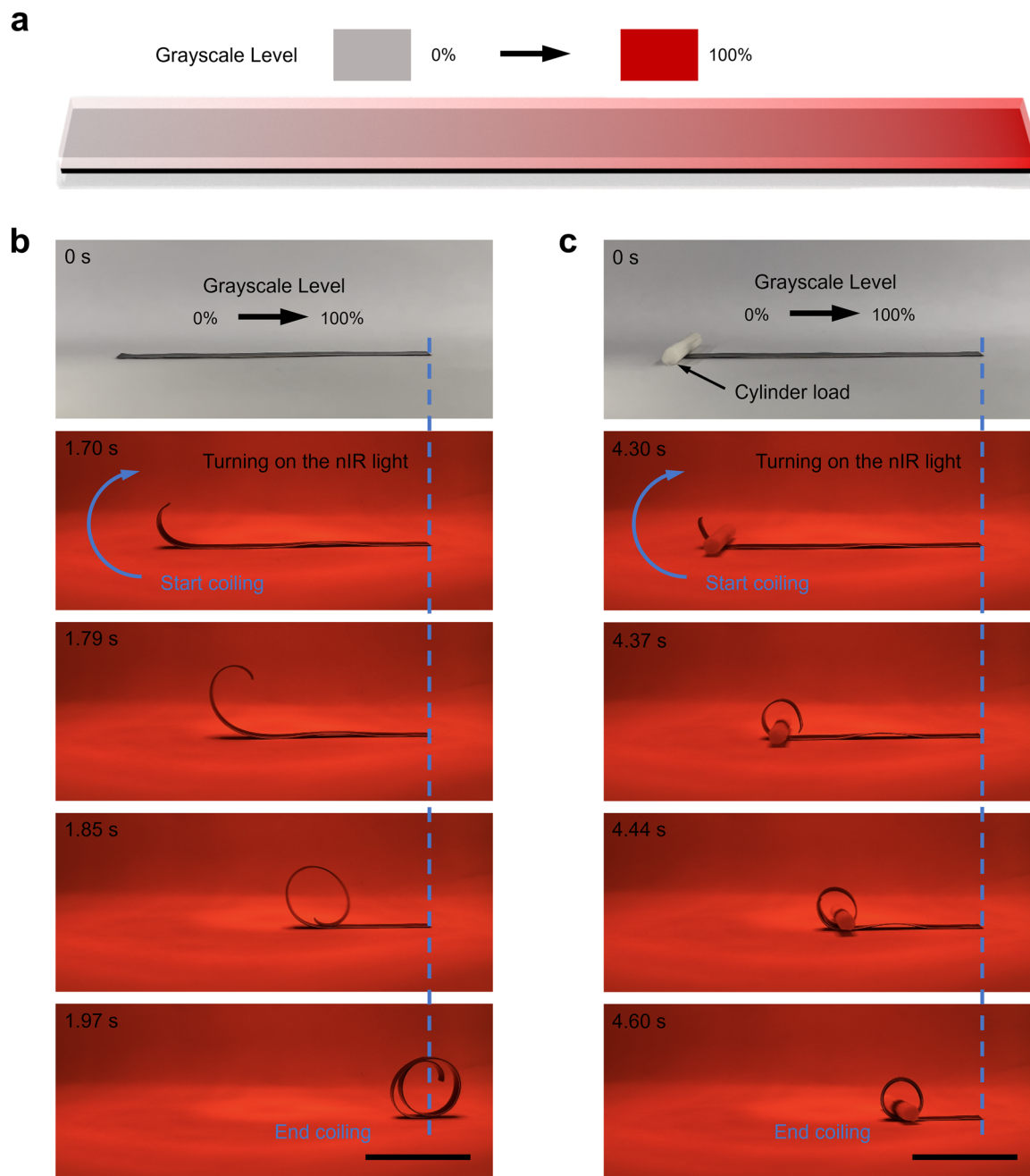
Fig. 7 Robotic arm inspired by an octopus arm, demonstrating coiling behavior under global heating using an nIR light. (a) Pattern and structure of the robotic arm. Snapshots showing (b) the coiling process of the robotic arm and (c) the arm coiling a load 15 times heavier than its own weight. Scale bars: 20 mm. The LCE layer was facing upward.

3. Conclusions

In short, the reported SPSAs are capable of precisely encoding different bending curvatures under a global thermal stimulus within a single actuator. Through a scalable grayscale ultraviolet (UV) light processing method, regions with different Young's moduli can be encoded by the UV photomask, which in turn programs the different local actuation behaviors under a global thermal stimulus. The large bending curvature and programmability are enabled by leveraging the large negative actuation strain of LCE, the large positive CTE of PDMS, and the UV-controllable Young's modulus of BP–PDMS. Parametric studies reveal that the actuator's performance is highly dependent on the thickness ratio of its layers and the Young's modulus of BP–PDMS. The use of photomasks with varying grayscale levels during UV treatment allows for spatially controlled modulus profiles, enabling complex bending behaviors and improved actuator programmability. We further demonstrate that the SPSAs show promise in soft robotic systems.

They are able to replicate the locomotion patterns of caterpillars and the coiling behavior of octopus arms. The forward and backward crawling motions of the caterpillar-inspired robots are achieved by designing BP–PDMS patterns with modulated body curvatures. The octopus arm-inspired actuator, utilizing a linear gradient grayscale photomask, demonstrates the capability to transition between coiled and flat shapes, showcasing its potential in tasks requiring object manipulation. The reported SPSAs represent a significant advancement in spatially programmable soft actuators. The programmability offers a robust basis for the development of adaptive and multifunctional devices, particularly in the realm of soft robotics.

4. Experimental section

Fabrication of the LCE

The LCE samples were synthesized using an adapted thiol–acrylate Michael addition reaction method.[1,45] The liquid crystal mesogenic monomer, specifically 1,4-bis-[4-(3-acryloyloxypropyloxy)benzoyloxy]-2-methylbenzene (RM 257, Ambeed Incorporated), was used without modification. The synthesis procedure was initiated by fully dissolving 2 g of RM 257 in 0.7 g of toluene (Sigma-Aldrich) at 85 °C and the solution was cooled at room temperature for 1 min. Subsequently, 0.42 g of the chain extender 2,2′-(ethylenedioxy)diethanethiol (EDDET, Sigma-Aldrich) and 0.18 g of crosslinker pentaerythritol tetrakis (3-mercaptopropionate) (PETMP, Sigma-Aldrich) were introduced into the solution. This mixture was thoroughly dissolved at 85 °C and then cooled at room temperature for 1 min. Further, 0.013 g of the photoinitiator (2-hydroxyethoxy)-2-methylpropiophenone (HHMP, Sigma-Aldrich) and 0.288 g of dipropyl amine (DPA, Sigma-Aldrich) solution (2 wt%, in toluene), serving as the catalyst, were added. The solution was mixed using a Vortex mixer (Thinky, AR-100) and degassed in a vacuum oven (Across International, E23F). Two glass slides, sprayed with the release agent (Smooth-On, Ease Release 205), were stacked with spacers, and the monomer solution was injected between them. The sample was left overnight to ensure a complete reaction. Subsequently, the glass slides were separated, and the sample was cured at 80 °C for 1 d. Upon full drying of the LCE ribbon, it underwent uniaxial stretching to achieve a strain of 100%, followed by exposure to 365-nm UV irradiation (Analytik Jena, CL-3000) for 30 min.

Fabrication of the photomask for treating the BP–PDMS

Different patterns were printed on sticker sheets (Silhouette) by an inkjet printer (HP, OfficeJet Pro 7740). These patterns were subsequently cut with a cutting machine (Silhouette, Cameo 4). The patterned stickers were then adhered to cover glasses with a thickness of 150 μm.

Fabrication of the BP–PDMS

BP (Sigma-Aldrich) was first dissolved in xylene (Sigma-Aldrich) at a concentration of 500 mg ml^{-1}. Subsequently, PDMS (Dow Corning, Sylgard 184), with a base-to-curing agent weight ratio

of 5 : 1, was mixed with the BP solution at a weight ratio of PDMS : BP = 20 : 1. The resulting BP–PDMS mixture was homogenized using a planetary mixer at 1000 rpm for 3 min. Then, a solution of poly(4-styrenesulfonic acid) (PSSA, Sigma-Aldrich) with a concentration of 18 wt% in DI water was coated onto a glass slide using a spin coater (Laurell Technologies, WS-650Mz-23NPPB) at a speed of 800 rpm for 1 min. After air-drying the PSSA-coated slide, the BP–PDMS mixture was spin coated onto the slide. The BP–PDMS was then selectively exposed to the 365-nm UV irradiation (Analytik Jena, CL-3000) through a photomask for 2 h, followed by thermally cured at 120 °C for 3 h on a hotplate. Note, the grayscale level was controlled by adjusting the transmittance of the photomask to the UV light. Ultimately, the BP–PDMS layer was obtained by immersing the cured BP–PDMS sample in water overnight at room temperature to remove the sacrificial PSSA layer.

Fabrication of the SPSA

Amorphous graphite powder (particle size: 44 μm, Fasco Epoxies) was mixed with PDMS at a base-to-curing agent weight ratio of 20 : 1. Release agent (Smooth-On, Ease Release 205) was then sprayed onto a Petri dish. Subsequently, the gPDMS mixture was spin coated onto the treated Petri dish and cured on a hotplate at 60 °C for 3 h.

Assembly of the SPSA

The SPSA was assembled through a layer-by-layer lamination process. Initially, the gPDMS layer and BP–PDMS layer were plasma treated (PIE Scientific, Tergeo) for 3 min. Following treatment, both layers were rinsed with water, laminated together, and carefully removed to eliminate air bubbles. The laminated layers were then dried at room temperature for 3 h. Subsequently, the other side of the gPDMS layer and the LCE layer were plasma treated for 3 min. The LCE layer was similarly laminated to the gPDMS layer under water and dried at room temperature for 3 h.

Actuation method of the SPSA

Two actuation methods were employed to activate the SPSA. To examine the effect of each layer's thickness on bending curvature as a function of temperature, samples with two free ends were placed in an oven. To investigate the programmability of the SPSA with different spatially programmed patterns, the samples were heated using a nIR lamp (GE, 250 W), at an intensity of 1430 mW cm^{-2}, which was positioned 10 cm above the sample. The SPSA was then allowed to cool at room temperature. Different recovery temperatures lead to different recovery rates (Fig. S12, ESI†). In all cases, the overall shape can be completely restored. The highest recovery rate was observed at 13 °C. For the following experiments, room temperature was used as the recovery temperature to simplify the experimental setup but still achieve a fast recovery rate.

Characterizations

A material testing system (MTS, 858 Mini Bionix II) was used to conduct stress–strain measurements. Samples of BP–PDMS,

gPDMS, and LCE were cut to a length of 10 mm and subjected to a strain of 50% at a rate of 0.01 mm s^{-1}. Stress values were determined by dividing the tensile force by the cross-sectional area of the samples. Strain values were calculated by dividing the distance by the initial sample length. For transmittance measurements, photomasks with grayscale levels of 0%, 10%, 15%, 20%, 30%, 60%, 90%, and 100%, each with dimensions of 15 mm by 15 mm, were prepared using the previously described method. The transmittance of these photomasks was measured using UV-vis Spectroscopy (Thermal Scientific, Genesys 30). Transmittance values were determined by averaging the results from three independent measurements. For temperature measurements, gPDMS samples, cut to dimensions of 50 mm by 50 mm, were exposed to nIR irradiation from an nIR lamp (GE, 250 W) positioned at a distance of 10 cm. The temperature of the gPDMS layer was recorded using an infrared temperature camera (FLIR, A325sc).

Author contributions

Y. L. and S. Y. conceived the project. Y. L. and S. N. C. fabricated the actuators and performed the experiments. Y. L., S. N. C., S. C., P. D., S. L., and S. Y. participated in discussions and data analysis. Finally, Y. L. and S. Y. wrote the manuscript with contributions from all the authors. S. Y. supervised this project.

Data availability

The data supporting this article have been presented in the manuscript and the ESI.†

Conflicts of interest

The authors declare no conflict of interest.

Acknowledgements

References

1 S. Wu, Y. Hong, Y. Zhao, J. Yin and Y. Zhu, *Sci. Adv.*, 2023, **9**, eadf8014.

2 C. Zhang, G. Chen, K. Zhang, B. Jin, Q. Zhao and T. Xie, *Adv. Mater.*, 2024, **36**, 2313078.

3 A. Kotikian, C. McMahan, E. C. Davidson, J. M. Muhammad, R. D. Weeks, C. Daraio and J. A. Lewis, *Sci. Robot.*, 2019, **4**, eaax7044.

4 Y. Wang, M. Li, J.-K. Chang, D. Aurelio, W. Li, B. J. Kim, J. H. Kim, M. Liscidini, J. A. Rogers and F. G. Omenetto, *Nat. Commun.*, 2021, **12**, 1651.

5 C. Song, Y. Zhang, J. Bao, Z. Wang, L. Zhang, J. Sun, R. Lan, Z. Yu, S. Zhu and H. Yang, *Adv. Funct. Mater.*, 2023, **33**, 2213771.

6 Q. Li, C. Liu, Y.-H. Lin, L. Liu, K. Jiang and S. Fan, *ACS Nano*, 2015, **9**, 409–418.

7 Y. Li, A. Halwah, S. R. Bhuiyan and S. Yao, *ACS Appl. Mater. Interfaces*, 2023, **15**, 58839–58849.

8 S. Chen, L. Yu, W. Shen, B. Fong, Y. Li, P. Dong, H. Qin and S. Yao, *Adv. Funct. Mater.*, 2024, **34**, 2314515.

9 J. Liu, Y.-S. Huang, Y. Liu, D. Zhang, K. Koynov, H.-J. Butt and S. Wu, *Nat. Chem.*, 2024, **16**, 1024.

10 R. C. P. Verpaalen, M. G. Debije, C. W. M. Bastiaansen, H. Halilović, T. A. P. Engels and A. P. H. J. Schenning, *J. Mater. Chem. A*, 2018, **6**, 17724.

11 D. Rus and M. T. Tolley, *Nature*, 2015, **521**, 467.

12 M. Li, A. Pal, A. Aghakhani, A. Pena-Francesch and M. Sitti, *Nat. Rev. Mater.*, 2022, **7**, 235–249.

13 C. Laschi, B. Mazzolai and M. Cianchetti, *Sci. Robot.*, 2016, **1**, eaah3690.

14 N. El-Atab, R. B. Mishra, F. Al-Modaf, L. Joharji, A. A. Alsharif, H. Alamoudi, M. Diaz, N. Qaiser and M. M. Hussain, *Adv. Intell. Syst.*, 2020, **2**, 2000128.

15 H. Wei, Q. Zhang, Y. Yao, L. Liu, Y. Liu and J. Leng, *ACS Appl. Mater. Interfaces*, 2017, **9**, 876–883.

16 D. W. Kim, Y. Hagiwara, S. Hasebe, N. O. Dogan, M. Zhang, T. Asahi, H. Koshima and M. Sitti, *Adv. Funct. Mater.*, 2023, **33**, 2305916.

17 Y. Dong, J. Wang, X. Guo, S. Yang, M. O. Ozen, P. Chen, X. Liu, W. Du, F. Xiao and U. Demirci, *Nat. Commun.*, 2019, **10**, 4087.

18 J. Jiang, Y. Ma, R. Cheng and Y. Zhao, *Adv. Funct. Mater.*, 2023, **34**, 2313625.

19 P. Du, X. Lin and X. Zhang, *Sens. Actuators, A*, 2010, **163**, 240.

20 M. Zhang, A. Pal, X. Lyu, Y. Wu and M. Sitti, *Nat. Mater.*, 2024, **23**, 560.

21 M. Ha, G. S. Cañón Bermúdez, J. A. C. Liu, E. S. Oliveros Mata, B. A. Evans, J. B. Tracy and D. Makarov, *Adv. Mater.*, 2021, **33**, 2008751.

22 Q. He, Z. Wang, Y. Wang, A. Minori, M. T. Tolley and S. Cai, *Sci. Adv.*, 2019, **5**, eaax5746.

23 L. Yue, X. Sun, L. Yu, M. Li, S. M. Montgomery, Y. Song, T. Nomura, M. Tanaka and H. J. Qi, *Nat. Commun.*, 2023, **14**, 5519.

24 X. Li, Y. Du, C. Xiao, X. Ding, X. Pan, K. Zheng, X. Liu, L. Chen, Y. Gong and M. Xue, *Adv. Funct. Mater.*, 2023, **34**, 2310380.

25 G. Cai, J.-H. Ciou, Y. Liu, Y. Jiang and P. S. Lee, *Sci. Adv.*, 2019, **5**, eaaw7956.

26 L. Zhang, J. Pan, Y. Liu, Y. Xu and A. Zhang, *ACS Appl. Mater. Interfaces*, 2020, **12**, 6727–6735.

27 B. Jin, H. Song, R. Jiang, J. Song, Q. Zhao and T. Xie, *Sci. Adv.*, 2018, **4**, eaao3865.

28 T. H. Ware, M. E. McConney, J. J. Wie, V. P. Tondiglia and T. J. White, *Science*, 2015, **347**, 982.

29 Z. C. Jiang, Y. Y. Xiao, X. Tong and Y. Zhao, *Angew. Chem., Int. Ed.*, 2019, **131**, 5386.

30 R. Yang and Y. Zhao, *Angew. Chem., Int. Ed.*, 2017, **129**, 14390.

31 Y. Yang, X. Zhang, C. Valenzuela, R. Bi, Y. Chen, Y. Liu, C. Zhang, W. Li, L. Wang and W. Feng, *Matter*, 2024, **7**, 2091–2107.

32 T. S. Hebner, R. G. Bowman, D. Duffy, C. Mostajeran, I. Griniasty, I. Cohen, M. Warner, C. N. Bowman and T. J. White, *ACS Appl. Mater. Interfaces*, 2023, **15**, 11092–11098.

33 J. Hu, Z.-Y. Kuang, L. Tao, Y.-F. Huang, Q. Wang, H.-L. Xie, J.-R. Yin and E.-Q. Chen, *ACS Appl. Mater. Interfaces*, 2019, **11**, 48393–48401.

34 D. Sezen Polat, V. E. Buurman, D. J. Mulder and D. Liu, *Chem. – Eur. J.*, 2024, **30**, e202400515.

35 H. Kim, H. Lee, I. Ha, J. Jung, P. Won, H. Cho, J. Yeo, S. Hong, S. Han and J. Kwon, *Adv. Funct. Mater.*, 2018, **28**, 1801847.

36 S. Yao, J. Cui, Z. Cui and Y. Zhu, *Nanoscale*, 2017, **9**, 3797.

37 Y. Chen, C. Valenzuela, X. Zhang, X. Yang, L. Wang and W. Feng, *Nat. Commun.*, 2023, **14**, 3036.

38 E. Sachyani Keneth, G. Scalet, M. Layani, G. Tibi, A. Degani, F. Auricchio and S. Magdassi, *Soft Robot.*, 2020, **7**, 123.

39 X. Wang, N. Jiao, S. Tung and L. Liu, *ACS Appl. Mater. Interfaces*, 2019, **11**, 30290–30299.

40 W. Wang, C. Li, M. Cho and S.-H. Ahn, *ACS Appl. Mater. Interfaces*, 2018, **10**, 10419–10427.

41 S. Wang, Y. Gao, A. Wei, P. Xiao, Y. Liang, W. Lu, C. Chen, C. Zhang, G. Yang and H. Yao, *Nat. Commun.*, 2020, **11**, 4359.

42 A. Alofi and G. Srivastava, *Phys. Rev. B: Condens. Matter Mater. Phys.*, 2013, **87**, 115421.

43 J. H. Low, J. Goh, N. Cheng, P. Khin, Q. Han and C.-H. Yeow, Paris, France, 2020.

44 M. Cai, S. Nie, Y. Du, C. Wang and J. Song, *ACS Appl. Mater. Interfaces*, 2019, **11**, 14340–14346.

45 M. O. Saed, A. H. Torbati, D. P. Nair and C. M. Yakacki, *J. Visualized Exp.*, 2016, **107**, e53546.

46 G. Chen, B. Ma, Y. Chen, Y. Chen, J. Zhang and H. Liu, *Adv. Sci.*, 2024, **11**, 2306129.

47 Y. Chen, J. Yang, X. Zhang, Y. Feng, H. Zeng, L. Wang and W. Feng, *Mater. Horiz.*, 2021, **8**, 728–757.

48 I. Apsite, S. Salehi and L. Ionov, *Chem. Rev.*, 2021, **122**, 1349–1415.

49 D. S. Shah, J. P. Powers, L. G. Tilton, S. Kriegman, J. Bongard and R. Kramer-Bottiglio, *Nat. Mach. Intell.*, 2021, **3**, 51.

50 Y. Gutfreund, T. Flash, Y. Yarom, G. Fiorito, I. Segev and B. Hochner, *J. Neurosci.*, 1996, **16**, 7297.

51 Y. Srinivasa and J. Mohanraju, *J. Insect Behav.*, 2011, **24**, 488.

52 B. C. Jayne, *Integr. Comp. Biol.*, 2020, **60**, 156.

53 S. Hanassy, A. Botvinnik, T. Flash and B. Hochner, *Bioinspiration Biomimetics*, 2015, **10**, 035001.